Coherent Steering of Nonlinear Chiral Valley Photons with Synthetic Au-WS$_2$ Metasurface

Guangwei Hu[1†], Xuanmiao Hong[2†], Kai Wang[2*], Jing Wu[3], He-Xiu Xu[1], Wenchao Zhao[2], Weiwei Liu[2], Shuang Zhang[4], Francisco Garcia-Vidal[5,6], Bing Wang[2], Peixiang Lu[2,7*], Cheng-Wei Qiu[1*]

[1]Department of Electrical and Computer Engineering, National University of Singapore, 4 Engineering Drive 3, Singapore 117583, Singapore

[2]Wuhan National Laboratory for Optoelectronics and School of Physics, Huazhong University of Science and Technology, Wuhan 430074, China

[3]Institute of Materials Research and Engineering, A*STAR (Agency for Science, Technology and Research), 2 Fusionopolis Way, Innovis, #08-03, 138634, Singapore

[4]School of Physics and Astronomy, University of Birmingham, Birmingham B15 2TT, UK

[5]Departamento de Física Teórica de la Materia Condensada and Condensed Matter Physics Center (IFIMAC), Universidad Autónoma de Madrid, E-28049 Madrid, Spain

[6]Donostia International Physics Center (DIPC), E-20018 Donostia/San Sebastian, Spain

[7]Laboratory of Optical Information Technology, Wuhan Institute of Technology, Wuhan 430205, China

[†]These authors contributed equally: Guangwei Hu and Xuanmiao Hong

*Corresponding authors:

Kai Wang, kale_wong@hust.edu.cn

Peixiang Lu, lupeixiang@hust.edu.cn

Cheng-Wei Qiu, chengwei.qiu@nus.edu.sg

Abstract

Two-dimensional transition-metal dichalcogenides (TMDCs) exhibit extraordinary nonlinearities and direct bandgaps at K (K') valleys. Those valleys could be optically manipulated through the plasmon-valley-exciton coupling, for example, with spin-dependent photoluminescence. However, the weak coherence between the pumping and emission due to intervalley scattering poses formidable challenges in exploring the valley-contrasting physics and applications. Here we show that a synthetic metasurface entangling the phase and spin of light can simultaneously enhance and manipulate the nonlinear valley-locked chiral emission in monolayer tungsten disulfide (WS_2) at room temperature. The second-harmonic valley photons, accessed and coherently pumped by the light with spin-related geometric phase imparted by Au-metasurface, are separated and routed to pre-determined directions in free space. Besides, the nonlinear photons with the same spin of incident light can be steered into any predefined direction thanks to the nonlinear optical selection rule of WS_2 in our synthetic metasurface. Our synthetic TMDCs-metasurface interface may facilitate advanced room-temperature and free-space nonlinear, quantum and valleytronic nanodevices.

Valleytronic and nanophotonic devices are two highly promising candidates to overcome the intrinsic heat issues of traditional optoelectronic chips. The valley corresponds to the extrema of the conduction and valence band continuum in the reciprocal space. To enable valleytronic devices, the fundamental requirement is to access the valley degree of freedom through their different responses of external stimuli such as electric, magnetic and optical means[1-3], which demands extremely challenging conditions such as low temperature. Recent studies on two-dimensional (2D) TMDCs have revealed that, due to the time-reversal symmetry and broken inversion symmetry, the degenerate K and K' valley in those materials with direct bandgap can respond distinctively to the spin angular momentum of light, exhibiting spin-valley-locked pumping, photoluminescence and even the nonlinear generation[4-7]. Various important applications in optoelectronics and valleytronics[4, 5, 8-13] are therefore realized. However, the lifetime of valley excited state is typically short[14], especially at room temperature, making it difficult to maintain the valley coherence and to manipulate the valley index. Moreover, the light-matter interaction is very weak in atomically thin TMDCs, and even weaker are the nonlinear optical frequency conversion processes. That seriously hinders the possibilities of nonlinear valleytronic devices based on 2D TMDCs[15-19]. Therefore, it is of great significance to establish viable approaches to boost the light interaction of those monolayers at room temperature and synthesize nanophotonics with valleytronic nonlinear devices for valley-multiplexed data transport. However, the auspicious opportunities are still rarely explored, prohibiting us from understanding and realizing many exciting valley-contrasting physics and applications by TMDCs.

Interestingly, optical metasurfaces[20, 21] with subwavelength meta-atoms have emerged as an important flat-profile platform in nanophotonics to fully manipulate the properties of light including phase, amplitude, spin, frequency, chirality, and etc. It enables various exciting applications such as metalenses[22, 23], metaholograms[24], carpet cloaking[25] and many others[26-29].

In particular, plasmonic metasurfaces with photonic spin-orbit interaction can discriminate the photonic spins and impart the spin-related geometric phase to light, where different spin components can be spatially split, known as photonic spin-Hall effect[30-35]. As a counterpart to free-space photonic spin-Hall metasurface, gratings with asymmetric corrugations or nanoholes[33-37] have been employed to launch unidirectional surface plasmon polaritons, which evanescently interact with 2D TMDCs in the near field. The consequent spin-dependent directional photoluminescence of the emission from those monolayer TMDCs[38, 39] serves as a straightforward evidence of the valley selection of monolayer TMDCs. However, the photoluminescence generation makes the coherence of the pumping and excited field so weak that valley excitonic emission can be barely manipulated for practical applications. This issue becomes more serious when simultaneously controlling the valley index in nonlinear regime and enhancing the spin-Hall effects from such monolayers in free space instead of near field.

Here, we theoretically propose and experimentally demonstrate a metasurface-assisted photonic pathway to boost the coherent spin-valley-dependent nonlinear optical process in monolayer TMDCs and to steer the nonlinear photons from different valleys to any desired directions in free space at room temperature. As shown in Fig. 1a, the synthetic Au-WS$_2$ metasurface contains two parts: the plasmonic gold (Au) metasurface (Fig. 1b), and the monolayer WS$_2$ atop it. In this synthetic metasurface, the intriguing spin-valley-exciton-locked second-harmonic generation (SHG) occurs exactly at the excitonic resonance of K and K' valleys in a monolayer WS$_2$[6, 12]. Due to the photonic spin-orbit interaction, the Au-metasurface will imprint a chirality-dependent gradient Pancharantnam-Berry phase[40-42] to the fundamental-frequency (FF) light , which pumps the coherent SHG process and, thus, steers nonlinear chiral photons emitted from different valleys to different directions (Fig. 1c). Furthermore, we also highlight here our metasurface can achieve 10-fold SH intensity enhancement thanks to the on-excitonic SHG and the large plasmonic field localization.

Principle of Steering Chiral Valley Nonlinear Photons

As shown in the differential distribution of SH chiral field in Fig. 1c, our metasurface can steer the nonlinear photons of opposite chirality, emitted from K and K' valleys, to different directions. Due to topological properties of broken inversion symmetry and D_{3h} ($\bar{6}m2$) symmetry of the monolayer WS$_2$, there will be complex interplay among the out-of-plane valley angular momentum, excitonic angular momentum, lattice angular momentum and the photon spin angular momentum in SHG according to the fundamental angular momentum conservation law[6]. Such an interplay results in the intriguing nonlinear selection rule[6, 12, 15], i.e. the counter-spin absorption and SHG as shown in Fig. 1d. This could also be understood mathematically, i.e. the second susceptibility tensor of D_{3h} point group has non-vanishing tensor components as

$$\chi_{aaa}^{(2)} = -\chi_{abb}^{(2)} = -\chi_{bba}^{(2)} = -\chi_{bab}^{(2)}$$

where *a* and *b* are the principal directions along armchair and zigzag direction, respectively. The multiplication of FF light with one spin will result in the SH photon with opposite spin (Supplementary Section 4). This selection rule is totally different from the incoherent photoluminescence process where the spin of absorbed and generated photons for one specific valley must be the same[4, 5, 43]. Therefore, although originating from the unique lattice symmetry of the WS$_2$ monolayer, the valley-contrasting physics from SHG is distinct from that of photoluminescence.

More importantly, the SHG is a coherent nonlinear process, which implies that the SH photons can be controlled by the manipulation of FF light. This lays the physical foundations of our synthetic An-WS$_2$ metasurface. As shown Fig. 1b, the Au metasurface is composed the rectangular nanohole arrays etched in gold film with the spatially varying rotation angle θ as

indicated in Fig 1e. Each nanohole forms an individual resonator (see Fig. S3 d-e) and can be treated as a birefringent waveplate[29] with the Jones' matrix expressed as

$$J(\theta) = T(-\theta) \begin{bmatrix} t_x & 0 \\ 0 & t_y \end{bmatrix} T(\theta)$$

where t_x and t_y denote the transmission along two orthogonal principal axes and $T(\cdot)$ is the rotation matrix (Supplementary Section 4). The Jones vector connects the output field ($\vec{E}^{out}$) and incident field ($\vec{E}^{inc}$) via the formula $\vec{E}^{out} = J(\theta) \cdot \vec{E}^{inc}$. Thus, the spin-dependent geometric phase due to the photonic spin-orbit interaction can be applied to the output FF field, which further excites the SHG from monolayer WS$_2$ atop the metasurface as illustrated in Fig. 1d. For example, the transmission of incident right-handed circularly polarized (RCP, $|+, \omega\rangle$) light through the unit cell will be divided in two parts: the residual RCP without geometric phase and left-handed circularly polarized (LCP, $|-, \omega\rangle$) light with geometric phase $e^{i2\theta}$. This will result in two components of coherent SHG ($P^{NL}(2\omega) \propto \chi^{(2)}[E(\omega)]^2$): the SH RCP light ($|+, 2\omega\rangle$) from K valley with double geometric phase $e^{i4\theta}$ and the SH LCP ($|-, 2\omega\rangle$) from K' valley without geometric phase. Thus, a spin-dependent gradient phase ($\nabla\phi$) arising from spatially varying rotation angle of unit cells could be imparted to the SH photons, which will provide the momentum matching to steer the valley photons to different directions according to generalized Snell's law[20, 30, 31], i.e. $k_x \hat{x} = \nabla\phi$. The theoretical details can be found in Supplementary Section 4. We lastly note that only in-plane chiral field ($E_x \hat{x} \pm iE_y \hat{y}$) can pump and interact with the valleys of 2D TMDCs effectively[43], which, as the matter of fact, are the ones our metasurface could achieve since the Jones' matrix operates on the x and y component of the incident field.

Experimental Demonstration of Steering Chiral Nonlinear Photons

For experimental verifications, the rectangular nanohole arranged in hexagonal lattice was fabricated by focused ion beam milling method (FEI Versa 3D). The thickness of the gold film is 60 nm; the periodicity of the nanohole array is 730 nm; the length and width of the rectangular etched nanohole is 335 nm and 145 nm, respectively. The rotation angle responsible for gradient phase in our metasurface is governed by $\partial_x \theta = \pi/\Lambda$, whose map is provided in supplementary Fig. S4a. Here, $\Lambda = 4.2$ μm is the spatial periodicity of the full π rotation angle variance. For determination of the degenerate valley band gap, the two-photon luminescence was performed and shown in supplementary Fig. S2, which is 2.004 eV in our case. The FF pumping energy is 1.002 eV. As partially described in Fig. 2e and the inserted illustrative schemes, a linearly polarized FF beam can be modified by a quarter-wave plate (QWP, WPQW-IR-4M, Sigma Koki, 1000 nm-1600 nm) for circular polarization generation. The FF beam focused by a lens (f=8 cm) pumps the sample, and then the emitted signal is collected by an objective lens (Olympus, 40× and 0.65 NA), filtered spectrally and imported to a spectrometer (Shamrock 303i, Andor) or a CMOS camera (Prime 95B, PHITIMETRICS) with a tube lens for imaging. For the propagation measurement, we captured the SHG signals at propagation planes from 0 to 200 μm along z-axis with the step 15 μm. The polarization of emitted SHG was extracted by a Glan-laser polarizer with a QWP (GL10-A and WPQ05M-633, Thorlabs) at z=120 μm. All optical measurements are done in room temperature. More details of the sample fabrication and optical measurement can be found in the Method.

Linearly Polarized (LP) Field Pumping We firstly test our synthetic metasurface with LP light (the QWP1 between laser and the sample is removed in this case). As the evolutionary light trajectory shown in xz plane Fig. 2e, the SHG is split to three beams, i.e. -1st, 0th and $+$1st orders. We can see that the intensity of -1st ($+$1st) order in image plane at propagation length z=120 um changes from strongest (nearly vanishing) when polarizer rotation angle (ψ) is 0 to vanishing (strongest) at $\psi = 90°$ and, finally, strongest (vanishing) when $\psi = 180°$,

while the 0th order remains unchanged. Such feature implies the opposite photon chiralities in above three orders and also matches the differential energy distribution ($I = I_{RCP} - I_{LCP}$, a.u.) in different image planes as shown in Fig. 1c. We also measured the intensity of LCP and RCP component of $-1st$, 0th and $+1st$ orders, shown in Fig. 2a-c respectively, which agrees with the result of spatial separation for different chiral photons. To characterize the figure of merit of accessing the valley via the metasurface in free space, the third Stokes parameter ($S_3 = \frac{I_{RCP} - I_{LCP}}{I_{RCP} + I_{LCP}}$, equivalent to the valley polarization considering the valley-locked nonlinear optical rules) at the valley-exciton binding energy is measured by the averaged photon counts per unit area of SHG spot. The measured S_3 of $-1st$, 0th and $+1st$ orders is -0.94, -0.16 and 0.88, respectively, indicating the nearly-perfect figure of merit. The minor deviation of S_3 from perfect CP ($S_3=\pm1$) or LP ($S_3=0$) could be the result of the oblique propagation of light and the experimental tolerance in measurements.

Very interestingly, in theory there should exist five spatial orders of SHG under LP incidence. The 0th order arises from the interference of SHG collaboratively excited by $|+, \omega\rangle$ and $|-, \omega\rangle$ without the geometric phase; the +1st order from the interference of SHG collaboratively excited by $|-, \omega\rangle$ with and without geometric phase; the +2nd order from the SHG excited only by $|-, \omega\rangle$ with geometry phase; the $-1st$ and -2nd orders are vice versa in spins. As a result, the deflection angle (α) of $\pm1st$ orders can be obtained by $k_{SHG} \sin \alpha = \pm\frac{2\pi}{\Lambda}$ while those of $\pm2nd$ orders are nearly doubled under small deflection angle governed by $k_{SHG} \sin \alpha' = \pm\frac{4\pi}{\Lambda}$, which is solely dependent on Λ. However, the intensity of higher order ($\pm2nd$) is much smaller due to the doubled steering angle associated with reduced diffraction efficiency and collection efficiency, which are therefore not reported here (Supplementary Section 4). In experiment, the steering angle of $\pm1st$ order is 8.5 degree, which agrees well with the theory. Moreover, the intensity ratio of the +1st, 0th and $-1st$ order is measured as 1.58:1:1.53, remarkably consistent

with the theoretical expectation of 1.59:1:1.59 ($2\left|t_x^2 - t_y^2\right|^2 : \left|t_x + t_y\right|^2 : 2\left|t_x^2 - t_y^2\right|^2$). The minor difference may come from the measurement error and the imperfection of fabrication. The exceptional agreement of the angle and the intensity ratio in experiment and theory in turn ascertains our proposed principle although our toy model simply neglects the complex near-field coupling between the metasurface and WS$_2$ monolayers.

Circularly Polarized Field Pumping We then switched the LP pumping to RCP ($\left|+, \omega\right\rangle$). A QWP would be placed between the linear polarizer and the synthetic metasurface in Fig. 2e. The experimental result of the SH intensity in different propagation length is shown in Fig. 3c. There are two significant orders which can be clearly observed—the 0$^{\text{th}}$ order of cross-polarized light ($\left|-, 2\omega\right\rangle$) emitted from K' valley and 1st order of co-polarized light ($\left|+, 2\omega\right\rangle$) emitted from K valley. The experimental measured S$_3$ are −0.99 and 0.94 respectively. Importantly, for conventional geometry-phase transmissive metasurface either linear (Fig. 3b) or nonlinear[31, 35, 44, 45], it is always the light with the opposite spin that are steered due to the spin conversion in spin-orbit interaction. However, our introduction of the valley degree of freedom of monolayer TMDCs with counter-spin SHG would allow the nonlinear photons with the same spins to be deflected as illustrated in Fig. 3a, which explicitly reveals the critical role of valley index in photonic spin-Hall process of metasurface.

Moreover, the other interesting feature is the spatial deflection angle of the 1st order (2α), which, counterintuitively, is approximately twice that of 1st order (α) when excited by LP light. Our measured result of the 1$^{\text{st}}$ order under CP pumping is 17.5 degree. This results from the residual co-polarized FF light without geometric phase under LP excitation. While the 1$^{\text{st}}$ order SHG under LP excitation comes from the interference of pumping K valley by the LCP light with geometric phase and the residual LCP component without geometric phase, the 1$^{\text{st}}$ order SHG under RCP excitation comes directly from the pumping of K valley solely by spin-

9

converted LCP component with geometric phase. In this way, one should expect the elimination of the residual co-polarized FF light without geometric phase if our meta-atom could satisfy the condition $|t_x| = |t_y|$ and $\angle t_y - \angle t_x = \pi$. This will consequently guarantee the same deflection angle of 1st order regardless of CP or LP pumping along with the disappearance of 0th order, which could further enhance the efficiency of our metasurface to selectively pump only one valley and route the SHG encoded with valley index into the free space.

Metasurface-enabled Plasmonic Enhancement of SHG

Finally, we report the other endearing advantages of metasurface, i.e. the plasmonic enhancement of SHG of monolayer TMDCs. The extraordinary second-harmonic nonlinearity of pure WS_2 has been reported as large as 5nm/V[15], several orders larger than traditional nonlinear photonic crystals. However, the few-atom thickness of monolayer TMDCs has significantly limited the nonlinear conversion efficiency, where novel approaches are in demand to boost the interactions. Fig. 4 compares the normalized SHG intensity of WS_2 on the plasmonic metasurface and the silica under the circularly polarized beam. One order enhancement of SHG intensity of monolayer WS_2 can be observed with Au metasurface, which could be attributed to two important factors. The first one is the valley excitonic-resonance in SHG generation, which echoes with reported findings of exciton-enhanced SHG[3, 13]. This effect is further demonstrated in Supplementary Section 7. The second one is the large local-field enhancement in the designed nanostructure due to the plasmonic resonance[46, 47] at FF as shown in Fig. S2c-d. Finite-difference time-domain simulations (see Methods section) further reveal the great plasmonic field enhancement at the metasurface-air interface, as indicated in Fig. S3 (e, f). This suggests that the SHG originated from the WS_2 are majorly contributed by plasmonic field confinement in nanohole area where light interaction with monolayer WS_2 is

strongly boosted. The theoretical estimation shows the averaged FF field enhancement $(|E_x(\omega)|^2 + |E_y(\omega)|^2)$ within the nanohole area is around 33, implying the SH field intensity in the hole area is 33^2 (~1000). Taking the area ratio of the nanohole into account (~0.1), the averaged SH field intensity enhancement can be estimated around tenfold ($\sim (33 \times 0.1)^2$) according to the normalization method discussed by Z. Wang *et al.*[46], which is reasonably large and also agrees well with both the experimental result shown in the Fig.4 and the rigorous nonlinear scattering theory (see Supplementary Section 6). Larger SHG intensity could be expected by topologically optimizing the nanostructure such as the length, thickness, width and other parameters, which is beyond our scope here since tenfold enhancement is fair enough to demonstrate the boosted light-matter interactions in our synthetic metasurface for nonlinear optical and optoelectronic applications[16]. We also remark that, not limited to our plasmonic metasurface, the Mie resonance in high-index and low-loss dielectric metasurface could also be potentially exploited in the future to boost nonlinear response of the 2D TMDCs[48-50].

Conclusions

In summary, we have proposed a synthetic metasurface hybridizing a plasmonic spin-Hall metasurface and WS$_2$ monolayer, which provides a photonic pathway to manipulate the valley-locked nonlinear emission and creates a nonlinear chiral valley-photon interface at room temperature. One order of magnitude enhancement in SHG is achieved due to the great near-field confinement of light, which could be further enhanced by in future. Besides, the photonic spin-orbit coupling can induce a chirality-related geometric phase that interacts with the different valleys of monolayer WS$_2$ and steer the nonlinear valley-exciton locked emission to any desired directions in free space, without resorting to any complicated external stimulus such as electric bias or magnetic field. Our strategy is of high fidelity and can be universally extended to other nanophotonic systems such as all-dielectric resonant metasurfaces and other

TMDC monolayers. The optical pumping or electron spin injection to prepare the valley could also be explored by our synthetic metasurface in the future. Our work could promise a distinct avenue to manipulate the valley exciton transport, steer the spin-valley-exciton emission with nonlinear chiral valley-photon interface, and encode the valley index into free space.

Reference

1. Xiao D., Yao W. & Niu Q. Valley-contrasting physics in graphene: magnetic moment and topological transport. *Phys. Rev. Lett.* **99,** 236809 (2007).

2. Yao W., Xiao D. & Niu Q. Valley-dependent optoelectronics from inversion symmetry breaking. *Phys. Rev. B* **77,** 235406 (2008).

3. Ross J. S. *et al.* Electrical control of neutral and charged excitons in a monolayer semiconductor. *Nat. Commun.* **4,** 1474 (2013).

4. Mak K. F., He K., Shan J. & Heinz T. F. Control of valley polarization in monolayer MoS_2 by optical helicity. *Nat. Nanotech.* **7,** 494-498(2012).

5. Zeng H., Dai J., Yao W., Xiao D. & Cui X. Valley polarization in MoS_2 monolayers by optical pumping. *Nat. Nanotech.* **7,** 490-493 (2012).

6. Xiao J. *et al.* Nonlinear optical selection rule based on valley-exciton locking in monolayer WS_2. *Light Sci. Appl.* **4,** e366 (2015).

7. Sun Z. *et al.* Optical control of room-temperature valley polaritons. *Nat. Photon.* **11**, 491-496 (2017).

8. Mak K. F., Lee C., Hone J., Shan J. & Heinz T. F. Atomically thin MoS_2: a new direct-gap semiconductor. *Phys. Rev. Lett.* **105**, 136805 (2010).

9. Novoselov K. S. *et al.* Two-dimensional atomic crystals. *Proc. Natl Acad. Sci. USA* **102,** 10451-10453 (2005).

10. Splendiani A., *et al.* Emerging photoluminescence in monolayer MoS_2. *Nano Lett.* **10**, 1271-1275 (2010).

11. Novoselov K. S., Mishchenko A., Carvalho A. & Castro Neto A. H. 2D materials and van der Waals heterostructures. *Science* **353,** aac9439 (2016).

12. Seyler K. L. *et al.* Electrical control of second-harmonic generation in a WSe_2 monolayer transistor. *Nat Nanotech.* **10**, 407-411 (2015).

13. Wang G. *et al.* Giant enhancement of the optical second-harmonic emission of WSe_2 monolayers by laser excitation at exciton resonances. *Phys. Rev. Lett.* **114,** 097403 (2015).

14. Selig M. *et al.* Excitonic linewidth and coherence lifetime in monolayer transition metal dichalcogenides. *Nat. Commun.* **7,** 13279 (2016).

15. Janisch C. *et al.* Extraordinary Second Harmonic Generation in tungsten disulfide monolayers. *Sci. Rep.* **4,** 5530 (2014).

16. Zhao M. *et al.* Atomically phase-matched second-harmonic generation in a 2D crystal. *Light Sci. Appl.* **5,** e16131 (2016).

17. Yu H., Cui X., Xu X., & Yao W. Valley excitons in two-dimensional semiconductors. *Natl Sci. Rev.* **2,** 57-70 (2015).

18. Mak K. F. & Shan J. Photonics and optoelectronics of 2D semiconductor transition metal dichalcogenides. *Nat. Photon.* **10**, 216-226 (2016).

19. Mak K. F., Xiao D. & Shan J. Light–valley interactions in 2D semiconductors. *Nat. Photon.* **12**, 451-460 (2018)

20. Yu N. *et al.* Light Propagation with Phase Discontinuities: Generalized Laws of Reflection and Refraction. *Science* **334,** 333-337 (2011).

21. Meinzer N., Barnes W. L. & Hooper I. R. Plasmonic meta-atoms and metasurfaces. *Nat. Photon.* **8**, 889-898 (2014).

22. Khorasaninejad M. *et al.* Metalenses at visible wavelengths: Diffraction-limited focusing and subwavelength resolution imaging. *Science* **352,** 1190-1194 (2016).

23. Chen X. *et al.* Dual-polarity plasmonic metalens for visible light. *Nat. Commun.* **3,** 1198 (2012).

24. Zheng G. *et al.* Metasurface holograms reaching 80% efficiency. *Nat. Nanotech.* **10,** 308-312 (2015).

25. Ni X., Wong Z. J., Mrejen M., Wang Y. & Zhang X. An ultrathin invisibility skin cloak for visible light. *Science* **349,** 1310-1314 (2015).

26. Lin D., Fan P., Hasman E.& Brongersma M. L. Dielectric gradient metasurface optical elements. *Science* **345,** 298-302 (2014).

27. Shitrit N. *et al.* Spin-optical metamaterial route to spin-controlled photonics. *Science* **340,** 724-726 (2013).

28. Tittl A. *et al.* Imaging-based molecular barcoding with pixelated dielectric metasurfaces. *Science* **360,** 1105-1109 (2018).

29. Arbabi A., Horie Y., Bagheri M. & Faraon A. Dielectric metasurfaces for complete control of phase and polarization with subwavelength spatial resolution and high transmission. *Nat. Nanotech.* **10,** 937-943 (2015).

30. Yin X., Ye Z., Rho J., Wang Y. & Zhang X. Photonic spin Hall effect at metasurfaces. *Science* **339,** 1405-1407 (2013).

31. Ling X. *et al.* Giant photonic spin Hall effect in momentum space in a structured metamaterial with spatially varying birefringence. *Light Sci. Appl.* **4,** e290 (2015).

32. Zhou J., *et al.* Broadband Photonic spin Hall meta-Lens. *ACS Nano* **12,** 82-88 (2018).

33. Lin J. *et al.* Polarization-controlled tunable directional coupling of surface plasmon polaritons. *Science* **340,** 331-334 (2013).

34. High A. A. *et al.* Visible-frequency hyperbolic metasurface. *Nature* **522**, 192-196 (2015).

35. Ling X. *et al.* Recent advances in the spin Hall effect of light. *Rep. Prog. Phys.* **80,** 066401 (2017).

36. Sattari H., Rashed A. R., Ozbay E., Caglayan H. Bright off-axis directional emission with plasmonic corrugations. *Opt. Express* **25,** 30827-30842 (2017).

37. Li D. *et al.* Unidirectional surface plasmon-polariton excitation by a compact slot partially filled with dielectric. *Opt. Express* **21,** 5949-5956 (2013).

38. Sun L. et al. Routing valley excitons in a monolayer MoS_2 with a metasurface. Preprint at https://arxiv.org/abs/1801.06543 (2018).

39. Chervy T. *et al.* Room temperature chiral coupling of valley excitons with spin-momentum ocked surface plasmons. *ACS Photonics* **5,** 1281-1287 (2018).

40. Bliokh K. Y., Rodríguez-Fortuño F. J., Nori F. & Zayats A. V. Spin–orbit interactions of light. *Nat. Photon.* **9,** 796-808 (2015).

41. Tan Q., Guo Q., Liu H., Huang X. & Zhang S. Controlling the plasmonic orbital angular momentum by combining the geometric and dynamic phases. *Nanoscale* **9,** 4944-4949 (2017).

42. Bomzon Z., Biener G., Kleiner V. & Hasman E. Space-variant Pancharatnam–Berry phase optical elements with computer-generated subwavelength gratings. *Opt. Lett.* **27,** 1141-1143 (2002).

43. Jones A. M. *et al.* Optical generation of excitonic valley coherence in monolayer WSe_2. *Nat. Nanotech.* **8,** 634-638 (2013).

44. Li G. *et al.* Continuous control of the nonlinearity phase for harmonic generations. *Nat. Mater.* **14,** 607-612 (2015).

45. Tymchenko M. *et al.* Gradient nonlinear Pancharatnam-Berry metasurfaces. *Phys. Rev. Lett.* **115,** 207403 (2015).

46. Wang Z. *et al.* Selectively Plasmon-enhanced second-harmonic generation from monolayer tungsten diselenide on flexible substrates. *ACS Nano* **12,** 1859-1867 (2018).

47. Chen J. *et al.* Tungsten disulfide–gold nanohole hybrid metasurfaces for nonlinear metalenses in the visible region. *Nano Lett.* **18,** 1344-1350 (2018).

48. Chen H. *et al.* Enhanced second-harmonic generation from two-dimensional MoSe2 on a silicon waveguide. *Light Sci. Appl.* **6,** e17060 (2017).

49. Kuznetsov A. I., Miroshnichenko A. E., Brongersma M. L., Kivshar Y. S. & Luk'yanchuk B. Optically resonant dielectric nanostructures. *Science* **354,** aag2472 (2016).

50. Cihan A. F., Curto A. G., Raza S., Kik P. G. & Brongersma M. L. Silicon Mie resonators for highly directional light emission from monolayer MoS_2. *Nat. Photon.* **12,** 284-290 (2018).
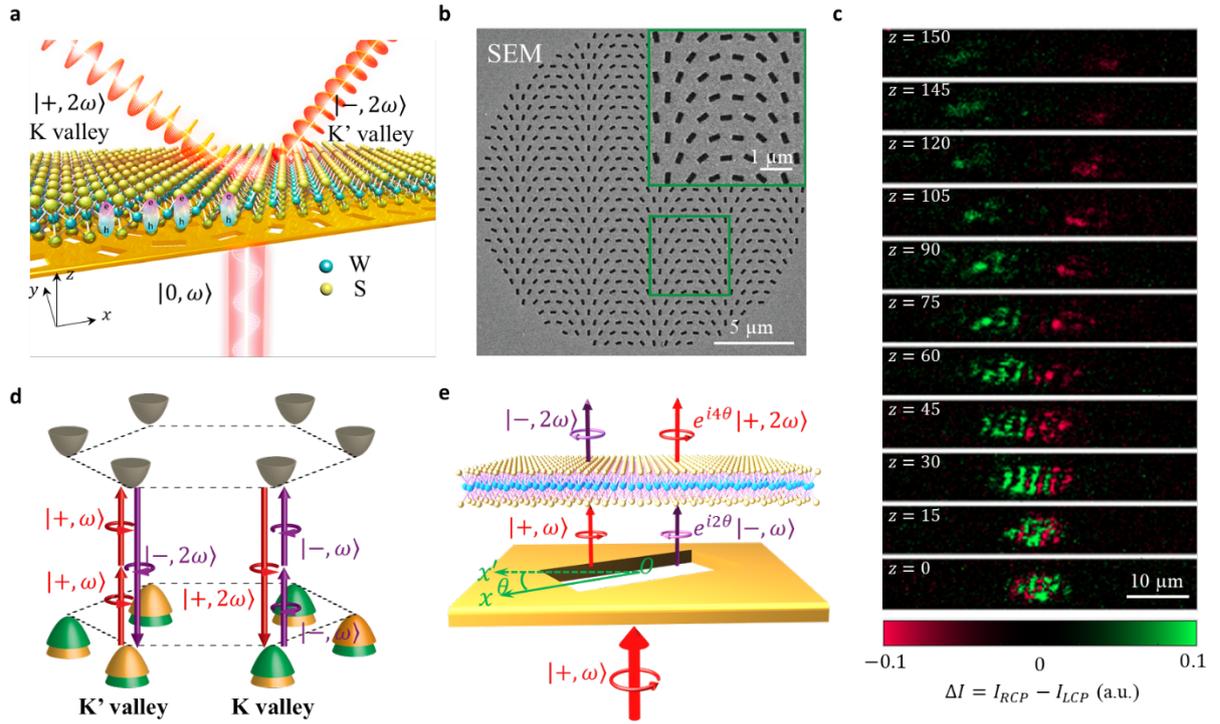
Fig.1 | Concept, major result and principle of the synthetic Au-WS$_2$ metasurface. a. Schematic of our synthetic Au-WS$_2$ metasurface. The single-layer WS$_2$ sits on top of gold metasurface. Upon the incident LP light ($|0,\omega\rangle$), the synthetic structure can yield large SHG from the valley band of the WS$_2$ and split opposite spin components of the SH valley-photons ($|+,2\omega\rangle$ and $|-,2\omega\rangle$) into different directions. **b**. SEM picture of photonic spin-Hall metasurface. It is composed of the rectangular nanoholes with different local rotation angles. **c**. The experimentally measured differential energy distribution and evolution of the SH signal along the propagation direction (z-direction, unit: μm) which is normalized by the maximum of the measured total intensity in the z=0 plane. **d**. The interband valley-exciton locked SHG selection rule. **e**. The schematic physics principle of the valley-photon interface in our hybridized structures. θ denotes the rotation angle with nanohole with respect to the x axis.
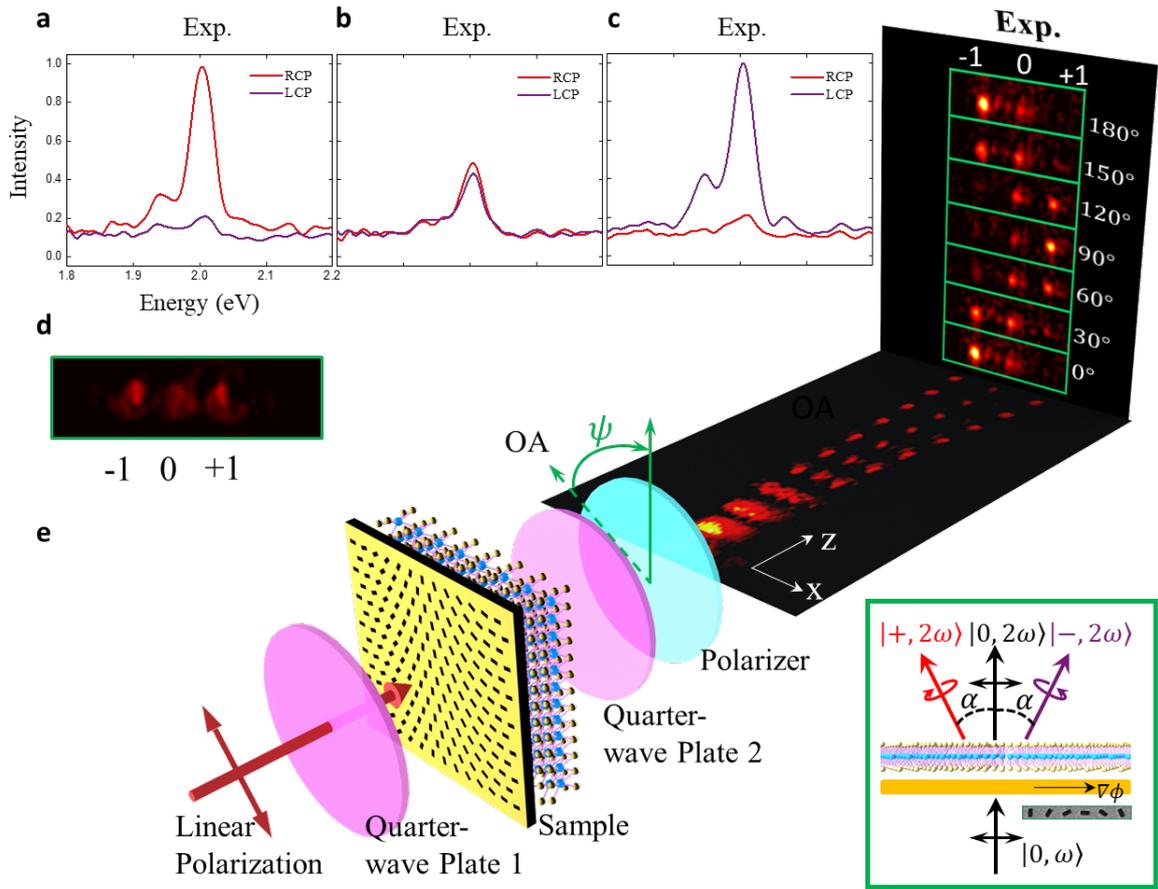
Fig. 2 | The experimental realization. **a-c**. The experimentally measured intensity of two chiral components (RCP and LCP) in the 1st, 0th and -1st orders, respectively, normalized by the maximum of the intensity of one spin component in that order. **d**. The field distribution in the CCD plane at z=120 μm with three obvious orders. It is measured without quarter-wave plate 2 (QWP2) and the polarizer. **e**. The schematic experimental optical setup. The incident beam is linearly polarized beam with the wavelength 1240 nm. The quarter-wave plate 1 (QWP1) can change the incident polarization to LP (without QWP1) or LCP or RCP component. The QWP2 and linear polarizer are exploited to test the chirality of the emitted SH photons. The bottom figure is the experimental result of evolution of the light splitting into three orders. The vertical embedded figures are the field distribution obtained by rotating the linear polarizer. The inset in right corner is the schematic illustration of the function of Au-WS$_2$ metasurface.
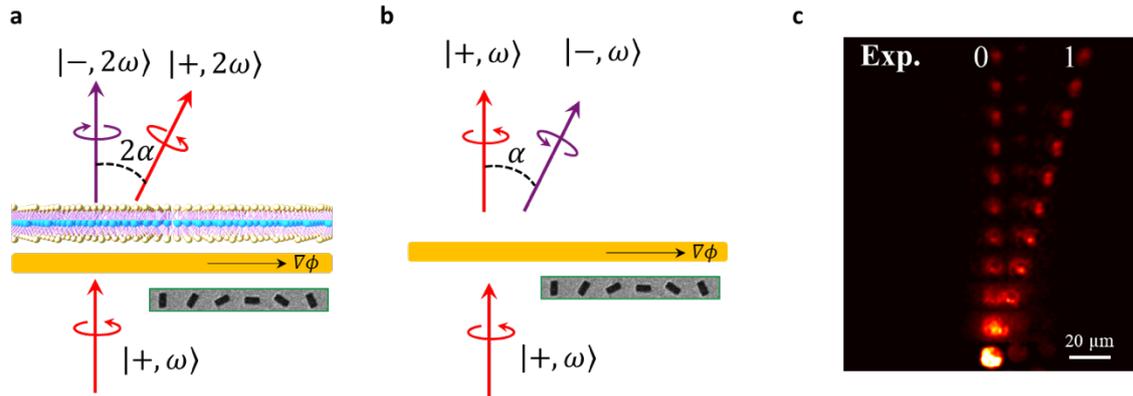
Fig. 3 | RCP pumping. **a, b**. The schematic representation of (**a**) steering SH waves upon RCP pumping with monolayer WS_2 and (**b**) photonic spin-Hall effect without WS_2. Different than the photonic spin Hall effect shown in **b**, the steered photon is the co-polarized component in hybridized structure in **a** with the double steering angle. The inserted SEM figures is one period of nanohole array in the range of Λ. **c**. The evolution of the light field for case **a**, as measured in the image plane at different propagation distances.
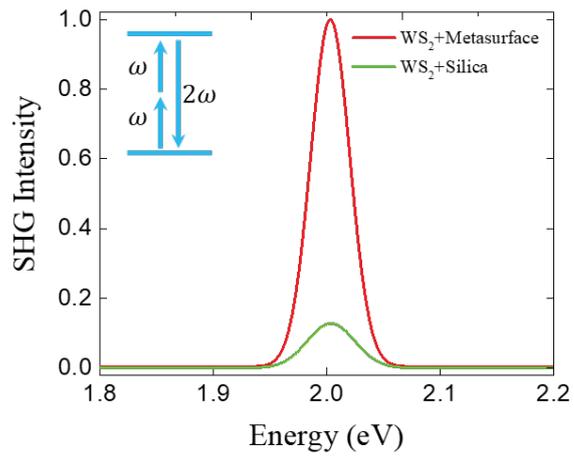
Fig. 4 | SHG enhancement in synthetic metasurface. The SHG signal from WS_2 on top of the Au metasurface (red line) and the silica (green line). The fundamental energy of excitation signal is 1.002eV.

Method

Sample fabrication. (1) The lift-off process of WS$_2$ monolayer. First, 1 g of polymethyl methacrylate (PMMA, Aldrich, average MW 996 000) was dissolved in anisole to prepare 50g of solution (2 wt%). A few drops of this solution were drop-coated on the sapphire substrate with WS$_2$ monolayer flakes until it fully covered the substrate. And then it was placed at room temperature for more than 1.5 h for the evaporation of the anisole, followed by curing step of baking at 120 °C for 0.5 h. Polymer strips (1 mm in width) were scratched by a blade at the edges of the substrate to reduce the lift-off time. The substrate was immersed in 3 mol/L NaOH aqueous solution at room temperature for more than 4h to etch the sapphire surface, and the PMMA-WS$_2$ films would lift off from the growth substrate naturally. The films were fished out with a glass slide and immersed in deionized water for 3 times in order to remove the residual NaOH solution. (2) The fabrication of gold metasurfaces. A 60-nm thick gold film with a 5-nm thick Cr adhesion layer was deposited on a quartz substrate by using an e-beam evaporator. The rectangular nanohole array was milled on the film by focused ion beam milling method (FIB, FEI Versa 3D). (3) The transfer process of the WS$_2$ monolayers. The PMMA-WS$_2$ films were fished out with the fabricated metasurfaces with a tweezers. Then it must be quickly aligned with the metasurface arrays under the microscope before the water is dried. The substrate was then baked at 120 °C for 1 h to improve the combination of WS$_2$ monolayers with the gold metasurfaces. Finally, the substrate was immersed in acetone for 3 times (each time 15 mins) to remove the PMMA film.

Optical measurement. (a) A mode-locked Ti-sapphire femtosecond laser system (Astrella Coherent, 35 fs, 800 nm and 1 kHz) and an optical parametric amplifier (TOPAS-Prime Plus, Light Conversion) were used as the fundamental beam at 1240 nm with a linear polarization. The polarization of the fundamental beam can further be adjusted by a QWP1 (WPQW-IR-4M, Sigma Koki, 1000 nm~1600 nm) for circular polarization generation. It was then focused by

an 8 cm lens to pump the sample for SHG. An objective (Olympus, 40× and 0.65 NA) was used to collect the emissions from the sample. After being filtered out the fundamental beam, the emitted signals were directly imported to a spectrometer (Shamrock 303i, Andor) or a CMOS camera (Prime 95B, PHITIMETRICS) with a tube lens for imaging. By moving the objective along z-axis, the images of the emitted signals were captured at the different planes along z-axis with a step of 15 μm. The polarization of emitted SH signal was extracted by a Glan-laser polarizer (GL10P-A, Thorlabs, 400 nm~700 nm) with a QWP2 at the SH wavelength (WPQ05M-633, Thorlabs). The axis of Glan-laser polarizer was set to be vertical (or horizontal) to extract the RCP and LCP components by rotating the fast-axis of the QWP2 at ±45°. The stokes parameters were determined by rotating the quarter-wave plate from 0° to 180° with a step of 10°.

Numerical simulation. The finite-difference time-domain simulation is performed by the commercial available software Lumerical Inc. (http://www.lumerical.com/tcad-products/fdtd/). The local field enhancement factor at the metasurface-air interface is obtained by taking the average of the electric field in the plane. The transmission coefficients along x and y direction are obtained by field of far-field monitor. The simulation result of transmission coefficient along two principal direction at the incident FF light is $t_x = 0.0961e^{2.1763i}$ and $t_y = 0.7183e^{-2.9896i}$. More details can be found in Supplementary Section.

Acknowledgements

Author Contributions

G.W.H., P.X.L., and C.W.Q. conceived the idea. K.W., P.X.L. and C.W.Q. supervised the project. G.W.H., K.W. and C.W.Q. designed the experiments. X.M.H, K.W., W.C.Z., W.W.L. and B.W. performed the experiments. G.W.H., J.W., K.W., H.X.X. S.Z., F. J. G.V., P.X.L. and C.W.Q. analyzed data. G.W.H. and C.W.Q. drafted the paper with the inputs from all authors.

Competing Interests: The authors declare no competing financial interests.

Data Availability: The data that support the plots within this paper and other findings of this study are available from the corresponding author upon reasonable request.